Proceedings of the ASME 2024 19th International Manufacturing Science and Engineering Conference
MSEC2024
June 17-21, 2024, Knoxville, Tennessee

MSEC2024-124112

SPATIAL ATOMIC LAYER DEPOSITION: REDUCED ORDER MODEL TOWARDS IN-LINE PROCESS CONTROL

Daniel Penley
University of Michigan
Ann Arbor, MI

Neil P. Dasgupta*
University of Michigan
Ann Arbor, MI

ABSTRACT

Spatial atomic layer deposition (SALD) is a thin film deposition technique that could provide precise atomic-scale control at a large enough scale for many applications, such as clean energy technologies, catalytic conversion, batteries, and anti-fouling coatings. The spatially separated precursor zones are sequentially exposed to the substrate surface to deposit a film with precise control. If the precursor zones were to intermix during a deposition process, the precise control over film thickness would be lost. Therefore, it is essential to control the location of the precursors within the process region during a manufacturing process. This is typically achieved by controlling the gas flow rates and/or pressures, however it is challenging to actively monitor the location of the precursors during a deposition process as the process region has a small characteristic length and the vapor/gas precursors are difficult to observe/monitor. Therefore, there is a need to validate the precursor location and consequential process quality during a deposition. This can be of particular importance for substrate surfaces that are highly irregular or for manufacturing conditions where external factors such as temperature and ambient air speeds could change dynamically. In this study, a reduced order COMSOL Multiphysics® model is introduced that can predict the location of precursors in the process region. The model itself is discussed; the mesh size is selected considering accuracy and computation time; the model outputs are shown; and an initial experimental validation of the model is demonstrated.

Keywords: spatial atomic layer deposition, computational model, process control, manufacturing

1. INTRODUCTION

Devices such as microprocessors, batteries, and displays have become nearly ubiquitous in everyday life. The performance of these devices depends on precise control and tuning of the varied surfaces and interfaces within the complex architectures. Improved performance is often achieved with enhanced control of the surface chemistry and geometry using micro- and nanoscale films. In a commercial setting, the semiconductor device fabrication industry has developed a range of tools and techniques to precisely engineer interfaces at the nanoscale. One such technique is atomic layer deposition (ALD), which enables continuous, conformal thin films on high-aspect ratio surfaces through sequential self-limiting chemical reactions that can be repeated cyclically to achieve desired thicknesses [1, 2].

Beyond semiconductor devices, many applications including clean energy technologies [3], catalytic conversion [4], batteries [5], and anti-fouling coatings [6] would benefit from the precise atomic-scale control that ALD offers. However, realizing these benefits at a commercial scale is difficult as these applications often require larger component volumes and surface areas compared to typical batch silicon wafer processing. Conventional ALD is typically performed at vacuum pressures with relatively slow cycle times, which limits the geometric scalability and lengthens process times, thus prohibitively increasing cost. These large-scale manufacturing challenges at the nanoscale restrict new advances realized in the laboratory from translating to industry.

A variant of conventional ALD, spatial atomic layer deposition (SALD) is a thin-film deposition technique that could perform the desired atomic-scale deposition within a large-scale manufacturing process. To achieve this scalability, SALD separates the precursors spatially into zones, rather than the temporally separated steps of conventional ALD [7–10]. Delivering the precursors in this manner enables SALD to be performed at atmospheric pressure, eliminating the need for vacuum systems and allowing for faster cycles times (~100x faster [11, 12]). Additionally, many SALD reactor designs have been reported for both batch [13–26] and roll-to-roll [13, 27] applications, demonstrating that they could be integrated into existing manufacturing processes. For this reason, SALD has enjoyed growing interest both experimentally [13–27] and computationally [16, 28–31].

Previously, we reported a customized, mechatronic SALD system that enables closed-loop control over the wide range of process parameters, which includes the gap size between the

*Corresponding author: ndasgupt@umich.edu

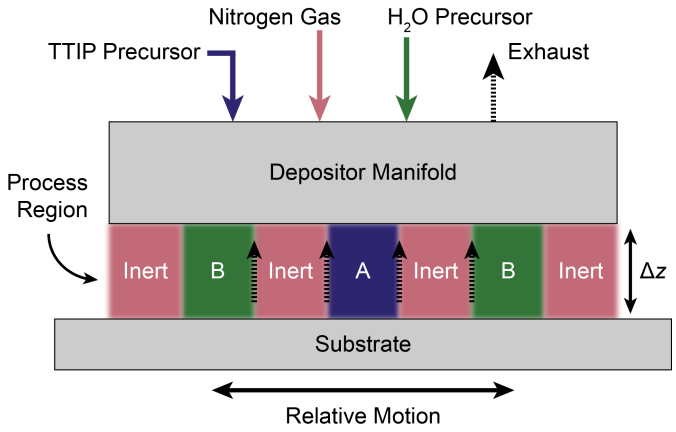

FIGURE 1: Simplified schematic of experimental SALD system showing the process region with precursor zones formed by the depositor manifold and substrate.

depositor and the substrate, the relative angular alignment of the depositor and substrate, the position and velocity of the substrate, the gas flow rates, and the temperature of the process [32]. As seen in Figure 1, the depositor creates zones of precursors to which a substrate is moved relative, exposing the substrate surface to the alternating precursors (A-B-A-B...). This sequential exposure allows for layer-by-layer deposition of the desired film. If the precursors were to exit their desired zone and enter the others, the substrate surface is exposed to precursors simultaneously and the growth rate of the thin-film deposition will be uncontrolled. As a result, the precise control of the deposited film will be lost.

Therefore, it is essential to ensure precursor containment throughout a deposition process. However, the process region is difficult to observe as the gap between the substrate and depositor is typically small (<1 mm) and the vapors/gases are optically transparent. Therefore, measuring or observing the fluid dynamics of the process region is difficult without significantly disrupting the process. To investigate computationally, we developed and reported a three-dimensional physics-based model to study the process region and the resulting film deposition maps [33]. The results of the fluid mechanics and precursor transport calculated in COMSOL Multiphysics® were inputted to Python 3 to solve the surface chemistry and predict the film deposition maps for a given set of process conditions.

While the three-dimensional model proved to be effective, the increased complexity of all three dimensions and the data transfer between software packages reduced the speed at which the model could generate meaningful results. Consequently, the previously reported model would not be able to be integrated into SALD manufacturing processes for in-line process control. This proposed model-informed process control would be beneficial for applications where the substrate surface topology is irregular or environmental factors are uncontrolled. If a numerical model were able to compute quickly enough, the model could aid with on-the-fly decision making as substrate surface geometries or environmental factors change dynamically. To this end, this study introduces a simplified two-dimensional numerical model to predict the location of precursor within the process region at speeds that could be realistic for a manufacturing context.

2. METHODS

The experimental system is equipped to perform titanium dioxide (TiO_2) deposition by creating isolated metal and oxidant precursor zones of titanium(IV) isopropoxide (TTIP) and de-ionized water (H_2O), respectively. COMSOL Multiphysics® was used to solve for the fluid dynamics using the Laminar Flow Physics package and for the precursor partial pressure gradients using the Transport of Diluted Species package. The model geometry was defined by the dimensions of the physical system, and the boundary conditions were established by the process parameters controlled by the mechatronic system. A mesh refinement process was performed to ensure accuracy while prioritizing speed.

2.1 Model Equations

The outputs of the Laminar Flow Physics package in COMSOL Multiphysics® are the pressure and velocity fields of the fluid flow region. The velocity field is then fed into the Transport of Diluted Species package to solve for the precursor partial pressure gradients. Both COMSOL Multiphysics® packages use a steady-state solver, assuming no time dependence on the results.

To solve the fluid mechanics, the Navier-Stokes equation (Equation 1) ensures conservation of momentum and is defined by

$$\rho(u \cdot \nabla u) = \nabla \cdot (-PI + \mu(\nabla u + (\nabla u)^T)) + F \tag{1}$$

where ρ is the fluid density, u is the fluid velocity, P is the fluid pressure, I is the identity matrix, μ is the dynamic viscosity, the superscript T denotes transpose, and F is any external force. Additionally, the continuity equation (Equation 2) maintains conservation of mass and is defined by

$$\rho \nabla \cdot (u) = 0 \tag{2}$$

where ρ is the fluid density and u is the fluid velocity.

To solve the precursor transport, the convection-diffusion equation (Equation 3) computes the convection transport and is defined by

$$\nabla \cdot J_i + u \cdot \nabla c_i = G_i \tag{3}$$

where J_i is the diffusion flux for species i, u is the fluid velocity, c_i is the concentration gradient for species i, and G_i are any source or sink terms for species i. It is assumed that there are no sources or sinks (G). The diffusive transport is calculated using Fick's law (Equation 4) and is defined as

$$J_i = -D_i \nabla c_i \tag{4}$$

where J_i is the diffusion flux for species i, D_i is the diffusion coefficient for species i, and c_i is the concentration gradient for species i. While the concentration gradients (c_i) are the software's defined output, it is typical to work with partial pressures (P_i) when studying gases, and in this study, the ideal gas law is used for this conversion.

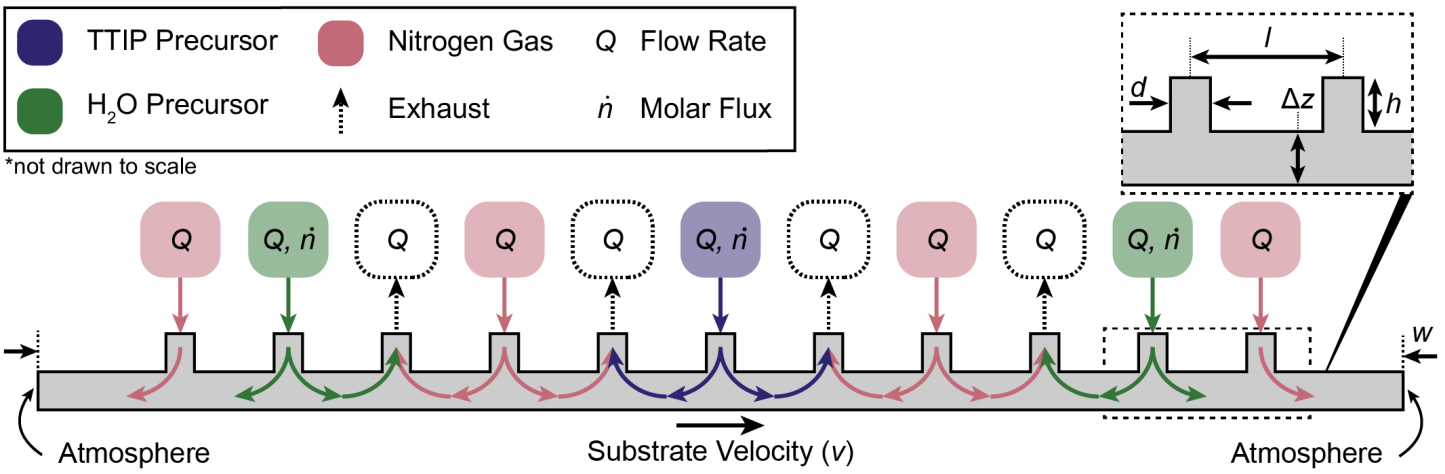

FIGURE 2: COMSOL model geometry of the SALD process region shown with dimensions and boundary conditions.

2.2 Model Geometry

The depositor and substrate on the experimental system form the three-dimensional process region, which contains the established precursor zones. A two-dimensional slice across the center of the precursor zones is taken to simplify the model geometry. The width of the process region (w in Figure 2) is set by the outer dimension of the depositor since the gas flow is uncontrolled beyond this point. The process region height is controlled by the gap size between the depositor and substrate surfaces (Δz in Figure 1 and Figure 2). Following a showerhead design, an array of pinholes on the bottom surface of the depositor is used to deliver the precursor vapors and nitrogen gas to the process region. The pinholes have a defined diameter (d in Figure 2) and center-to-center spacing (l in Figure 2). The height of the pinholes (h in Figure 2) is assumed to be smaller than those on the physical system to simplify the complex flow channels within the depositor manifold. The exact values for each geometric parameter can be found in Table 2 in Appendix A.

2.3 Boundary Conditions

The experimental system controls the gas flow rates via closed-loop control with mass flow controllers and a pressure regulator. The flow for each zone type is directed through the depositor manifold channels and delivered to the process region via an array of pinholes, similar to a showerhead. Within the model, the flow rate of each pinhole into or out of the process region is assigned to match that of a single pinhole on the experimental system (Figure 2).

To isolate the process region from the environment, the two outer nitrogen pinhole flows are primarily directed out of the process region ($Q_{N_2\text{-out}}$). The two inner nitrogen pinhole flows are designed to separate the metal and oxidant precursors ($Q_{N_2\text{-in}}$). Exhaust lines remove the excess precursor vapor and byproducts from the surface reaction (Q_{exh}). More details on the selection of the exhaust flow rate can be found in our prior experimental study [32].

The molar flux of precursor vapor ($\dot{n}$) delivered to the process region is controlled by the flow rate for the respective precursor. Nitrogen gas is directed through a liquid bubbler to generate

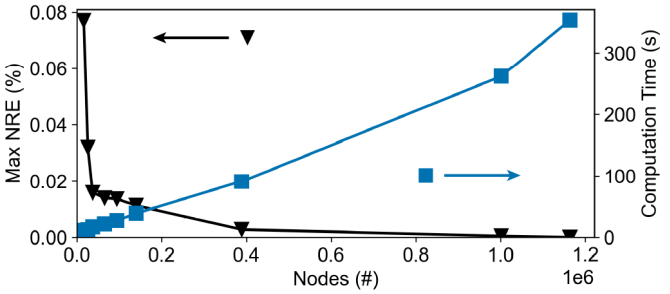

FIGURE 3: Mesh refinement plots showing the maximum normalized relative error (%) and computation time (sec) as a function of nodes within the mesh.

precursor vapors that are then driven to the process region. The TTIP and H_2O flow rates (Q_{TTIP} and Q_{H_2O}) control the flux of the respective precursor ($\dot{n}_{TTIP}$ and $\dot{n}_{H_2O}$). More details on the calculation of the precursor molar fluxes can be found in our prior experimental study [32].

At the beginning of each calculation, the entire fluid flow region is assumed to be at atmospheric pressure with no velocity and at a constant temperature (T). A no-slip condition is placed on the depositor walls and substrate surface. The substrate surface is modeled to move in a single direction with a constant velocity (v in Figure 2) with a wall velocity constraint. The portions of the process region that are open to the atmosphere are defined with zero normal stress as open boundaries. The diffusion coefficients of the precursors were calculated in another study [33]. For the boundary conditions parameter values, please see Table 2 in Appendix A.

2.4 Mesh Refinement

The simplification of the model geometry from three to two dimensions greatly reduces the complexity and resulting computation time. However, to develop a model that can provide reliable results at time scales meaningful to a manufacturing context, the selection of the mesh size is critical. If the mesh is too coarse, the results of the model may not be accurate, thus harming the

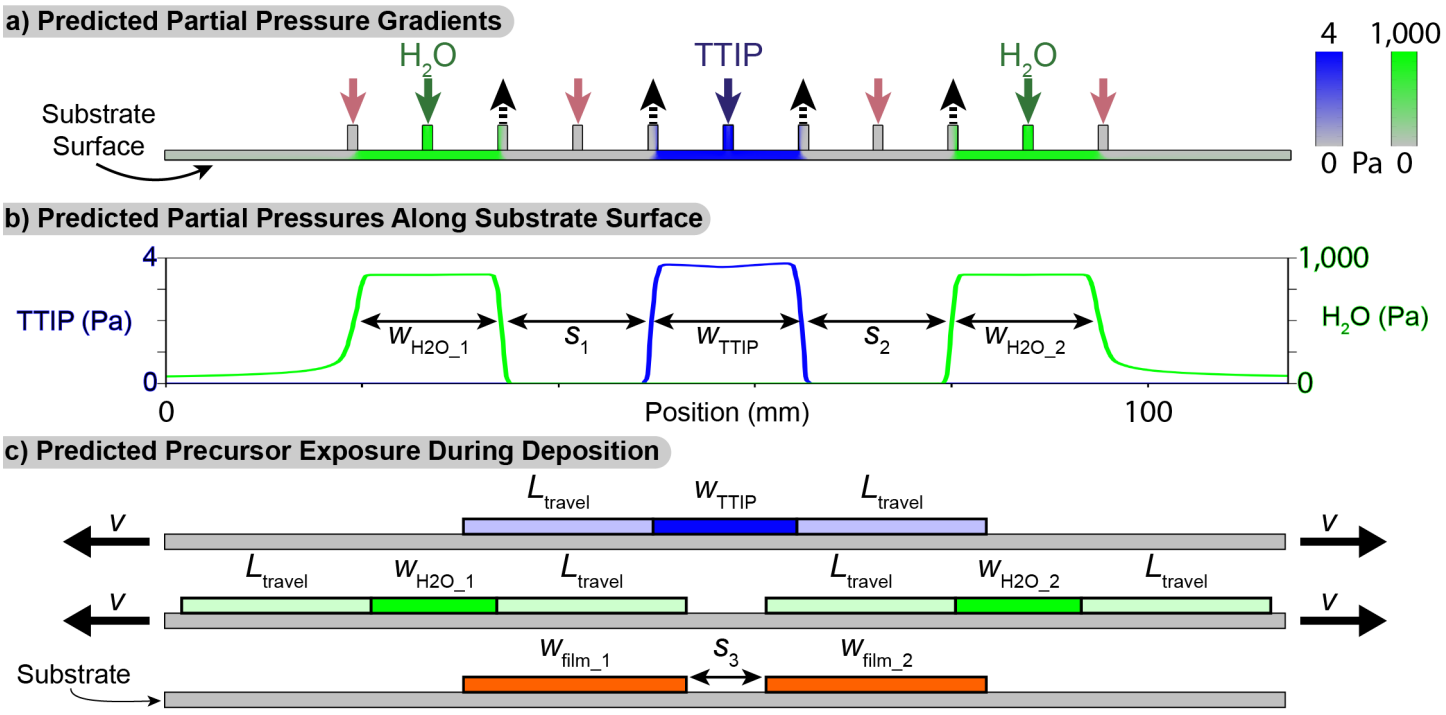

FIGURE 4: a) Predicted partial pressure gradient for TTIP (blue) and H_2O (green) and b) the corresponding predicted partial pressures along the substrate surface. TTIP (blue), left axis. H_2O (green), right axis. c) Predicted precursor exposure on the substrate surface during a deposition process with a travel length (L_{travel}) and substrate velocity (v), and the predicted film geometry based on the overlap of the precursor exposures.

real-time process control. But if the mesh is too fine, the time to solve may still be too long for functional results.

For the described model geometry, the built-in COMSOL Multiphysics® physics-dependent mesh builder was used to create varying sizes of meshes (Extremely Coarse to Extremely Fine) with a number of nodes corresponding to the fineness of the mesh. Each available mesh size was built and used to compute the model solution. The normalized relative error (NRE) for each mesh size was calculated with reference to the finest mesh using

$$NRE = \frac{X_i - X_{finest}}{max(X_{finest})} * 100 \quad (5)$$

where X_i is the result for parameter X using mesh i and X_{finest} is the result for parameter X using the finest mesh size. The NRE was calculated for each parameter of interest - total pressure, TTIP partial pressure, and H_2O partial pressure. The maximum NRE of the three parameters of interest was recorded as the error for each mesh size, shown in Figure 3. Additionally, the computation time for each mesh size is plotted against the number of nodes within the mesh.

The maximum error across all mesh sizes relative to the finest mesh is less than 0.08%, indicating that an increase of over 1 million mesh nodes only fractionally altered the result. Therefore, from an accuracy perspective, any of the meshes could be selected confidently. For the proposed in-line process control application, the fastest computation time is desired. Therefore, the coarsest mesh size (Extremely Coarse with ~16,000 nodes) was selected. With a computation time of approximately 11 sec, the numerical model can make predictions at a time-scale that is appropriate for in-line process control. While beyond the scope of this study, the number of mesh nodes could further be reduced to find a faster solution while still delivering reasonably accurate results.

3. RESULTS AND DISCUSSION

The model yields two-dimensional gradients of the fluid velocity and pressure and the precursor partial pressures. The values for the model parameters were established by experimental process conditions known to be well behaved on the physical SALD system. Since the location of the precursors is important for the deposition quality, the precursor partial pressure gradients are the focus of this study (Figure 4a). For a well-behaved SALD process, the precursors must be contained within their respective zone so that they are isolated from the other. If the precursors are exposed to the substrate surface concurrently, chemical vapor deposition (CVD) would occur, resulting in uncontrolled film growth and a loss of precise control. The precursor partial pressures along the substrate surface are plotted (Figure 4b).

3.1 Predicted Precursor Isolation

The TTIP precursor zone is established by the TTIP pinhole and the two exhaust lines on either side (Figure 2 and Figure 4a). The width of the TTIP precursor zone (w_{TTIP}) should approximately be the distance between the exhaust lines as they are designed to remove any excess precursor from the process region. The partial pressure of TTIP along the surface of the substrate is plotted in Figure 4b, and w_{TTIP} is predicted to be 19 mm. Within

the zone, the partial pressure deviates from the maximum by less than 3%, which is desirable for uniform surface exposure. More importantly, the partial pressure quickly drops to zero beyond the exhaust lines defining the TTIP zone. This indicates that the TTIP zone is expected to be well established for these process parameters since TTIP vapor is not exiting towards the H_2O zones. However, it must also be confirmed that the H_2O vapor is not entering into the TTIP zone.

While there is only one TTIP precursor zone, there are two H_2O zones with their own respective widths ($w_{H_2O\_1}$ and $w_{H_2O\_2}$). The boundaries of each are established by a single exhaust line and the outer nitrogen curtain. As seen in Figure 4b, the inner edges of the H_2O zones are well defined as the partial pressure drops to zero quickly towards the inside of the process region. However, the H_2O vapor is exiting the process region to the environment, as shown by the non-zero partial pressure at the edges of the process region. This does not pose any safety concerns for this process as H_2O vapor poses no health risk or environmental danger. If a precursor other than H_2O were used, further tuning of the process parameters would be needed to ensure containment within the process region. Because of the relative safety of H_2O and to generalize the analysis, the outer edges of the H_2O zones are assumed to correspond to the significant decrease in partial pressure. The widths $w_{H_2O\_1}$ and $w_{H_2O\_2}$ are predicted to be 16.5 mm and 16.7 mm, respectively. While these values are similar to each other for the given conditions, if the substrate velocity were to be higher, the widths of the two H_2O zones could have non-negligible differences. Similarly, the spaces between the TTIP and H_2O zones (s_1 and s_2) could be different in magnitude. However, for the modeled process parameters, s_1 and s_2 are predicted to be 11.5 mm and 11.8 mm, respectively.

3.2 Initial Experimental Validation

During a deposition process, the substrate is moved back-and-forth relative to the precursor zones along a defined travel length (L_{travel}) with a constant substrate velocity (v). As shown in Figure 4c, the region of the substrate surface that is exposed to each precursor increases as each zone edge is moved L_{travel}. In a well-behaved SALD process where the precursors are separated, deposition will only occur in the regions where the substrate surface is exposed to both precursors. The expected deposition widths (w_{film_1} and w_{film_2}) and the space between them (s_3) can be predicted with the zone widths (w_{TTIP}, $w_{H_2O\_1}$, and $w_{H_2O\_2}$), spacings (s_1 and s_2), and travel length (L_{travel}). The predicted deposited film geometric values are listed in Table 1.

Using the experimental SALD tool, 400 cycles of TiO_2 were deposited on a 6-inch silicon wafer using the parameters reported in Table 2. The direction of motion for the sample was left and right to be consistent with the schematic in Figure 4c. Two regions of deposited TiO_2 can be observed, which are consistent with the geometry predicted by the model (Figure 5). This indicates that the precursors are isolated in their respective zones. Additionally, the experimental deposition widths and interspacing are reported in Table 1. The experimentally measured w_{film_1} and w_{film_2} are smaller than the predicted values by ~13% and ~10% respectively, while the experimentally measured s_3 is larger than the predicted value by ~22%. While more work could be done to reduce the magnitude of the error, the general shape and scale of the predicted film is comparable to the experimental film. Further validation is needed and could include comparing predicted and experimental outcomes over a wide range of process parameters. Further discussion on the film features and geometry can be found in references [32, 33].

TABLE 1: Deposited Film Geometric Values

	w_{film_1}	s_3	w_{film_2}
Predicted (mm)	24.5	6.3	24.2
Experiment (mm)	21.3	7.7	21.8

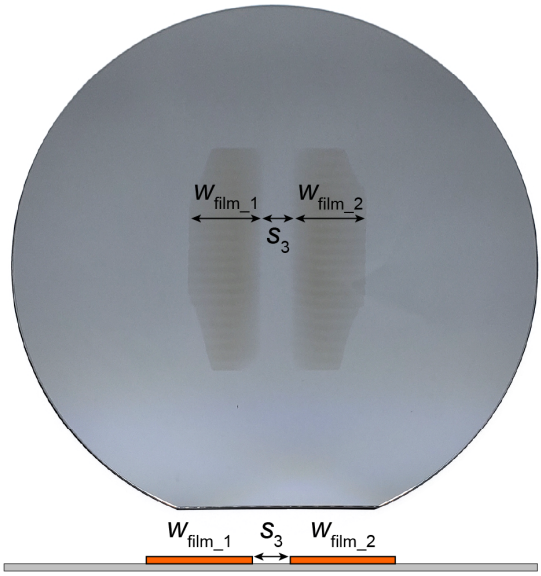

FIGURE 5: 400 cycles of deposited TiO_2 film on a 6-inch silicon wafer with labelled deposition widths and interspacing, and the predicted film geometry.

Additionally, the film thickness was measured using spectroscopic ellipsometry (Film Sense FS-1 Multi-Wavelength). The bulk film in each deposition region was measured to be ~23 nm thick. Therefore, the growth rate over the 400 ALD cycles was ~0.58 Å cycle^{-1}, which corresponds well with the previously reported 0.54 Å cycle^{-1} [32]. This finding further suggests the experimental system performed well-behaved ALD with isolated precursors.

4. CONCLUSION

A reduced order model in COMSOL Multiphysics® was developed to predict the location of precursor within the process region of an SALD system. The model speed and accuracy were considered to enable the use of the model for enhanced in-line process control, particularly for applications with irregular substrate surfaces and uncontrolled environmental factors. An initial validation of the model was demonstrated by comparing the geometry of the predicted and experimental films. Future work includes further experimental validation, such as varying the process parameters over a wide range of predicted and experimental outcomes, and integration with the mechatronic system to aid in manufacturing process control decisions.

ACKNOWLEDGMENTS

This material is based upon work supported by the National Science Foundation under Grants No. 1727918 and 1751590. The authors acknowledge the University of Michigan College of Engineering for financial support.

REFERENCES

[1] George, Steven M. "Atomic Layer Deposition: An Overview." *Chemical Reviews* Vol. 110 No. 1 (2010): pp. 111–131. DOI 10.1021/cr900056b. Accessed 2023-09-22, URL https://doi.org/10.1021/cr900056b. Publisher: American Chemical Society.

[2] Johnson, Richard W., Hultqvist, Adam and Bent, Stacey F. "A brief review of atomic layer deposition: from fundamentals to applications." *Materials Today* Vol. 17 No. 5 (2014): pp. 236–246. DOI 10.1016/j.mattod.2014.04.026. Accessed 2023-09-22, URL https://www.sciencedirect.com/science/article/pii/S1369702114001436. Publisher: Elsevier.

[3] A. Raiford, James, T. Oyakhire, Solomon and F. Bent, Stacey. "Applications of atomic layer deposition and chemical vapor deposition for perovskite solar cells." *Energy & Environmental Science* Vol. 13 No. 7 (2020): pp. 1997–2023. DOI 10.1039/D0EE00385A. Accessed 2023-11-16, URL https://pubs-rsc-org.proxy.lib.umich.edu/en/content/articlelanding/2020/ee/d0ee00385a. Publisher: Royal Society of Chemistry.

[4] Rodríguez, Robin E., Agarwal, Sneha P., An, Shun, Kazyak, Eric, Das, Debashree, Shang, Wen, Skye, Rachael, Deng, Tao and Dasgupta, Neil P. "Biotemplated Morpho Butterfly Wings for Tunable Structurally Colored Photocatalysts." *ACS Applied Materials & Interfaces* Vol. 10 No. 5 (2018): pp. 4614–4621. DOI 10.1021/acsami.7b14383. Accessed 2023-11-15, URL https://doi.org/10.1021/acsami.7b14383. Publisher: American Chemical Society.

[5] Kazyak, Eric, Chen, Kuan-Hung, Chen, Yuxin, Cho, Tae H. and Dasgupta, Neil P. "Enabling 4C Fast Charging of Lithium-Ion Batteries by Coating Graphite with a Solid-State Electrolyte." Vol. 12 No. 1 (2022): p. 2102618. DOI 10.1002/aenm.202102618. Accessed 2023-11-16, URL https://onlinelibrary.wiley.com/doi/10.1002/aenm.202102618.

[6] Wang, Jing, Lee, Sudarat, Bielinski, Ashley R., Meyer, Kevin A., Dhyani, Abhishek, Ortiz-Ortiz, Alondra M., Tuteja, Anish and Dasgupta, Neil P. "Rational Design of Transparent Nanowire Architectures with Tunable Geometries for Preventing Marine Fouling." *Advanced Materials Interfaces* Vol. 7 No. 17 (2020): p. 2000672. DOI 10.1002/admi.202000672. Accessed 2023-09-22, URL https://onlinelibrary.wiley.com/doi/abs/10.1002/admi.202000672. _eprint: https://onlinelibrary.wiley.com/doi/pdf/10.1002/admi.202000672.

[7] Suntola, Tuomo and Antson, Jorma. "Method for producing compound thin films." (1977). Accessed 2023-09-22, URL https://patents.google.com/patent/US4058430A/en.

[8] Suntola, Tuomo S., Pakkala, Arto J. and Lindfors, Sven G. "Apparatus for performing growth of compound thin films." (1983). Accessed 2023-09-22, URL https://patents.google.com/patent/US4389973A/en.

[9] Poodt, Paul, Cameron, David C., Dickey, Eric, George, Steven M., Kuznetsov, Vladimir, Parsons, Gregory N., Roozeboom, Fred, Sundaram, Ganesh and Vermeer, Ad. "Spatial atomic layer deposition: A route towards further industrialization of atomic layer deposition." *Journal of Vacuum Science & Technology A* Vol. 30 No. 1 (2011): p. 010802. DOI 10.1116/1.3670745. Accessed 2023-09-22, URL https://doi.org/10.1116/1.3670745.

[10] Hoye, Robert L. Z., Muñoz-Rojas, David, Nelson, Shelby F., Illiberi, Andrea, Poodt, Paul, Roozeboom, Fred and MacManus-Driscoll, Judith L. "Research Update: Atmospheric pressure spatial atomic layer deposition of ZnO thin films: Reactors, doping, and devices." *APL Materials* Vol. 3 No. 4 (2015): p. 040701. DOI 10.1063/1.4916525. Accessed 2023-09-22, URL https://doi.org/10.1063/1.4916525.

[11] Poodt, Paul, Lankhorst, Adriaan, Roozeboom, Fred, Spee, Karel, Maas, Diederik and Vermeer, Ad. "High-Speed Spatial Atomic-Layer Deposition of Aluminum Oxide Layers for Solar Cell Passivation." *Advanced Materials* Vol. 22 No. 32 (2010): pp. 3564–3567. DOI 10.1002/adma.201000766. Accessed 2023-09-22, URL https://onlinelibrary.wiley.com/doi/abs/10.1002/adma.201000766. _eprint: https://onlinelibrary.wiley.com/doi/pdf/10.1002/adma.201000766.

[12] Illiberi, A., Scherpenborg, R., Roozeboom, F. and Poodt, P. "Atmospheric Spatial Atomic Layer Deposition of In-Doped ZnO." *ECS Journal of Solid State Science and Technology* Vol. 3 No. 5 (2014): p. P111. DOI 10.1149/2.002405jss. Accessed 2023-09-22, URL https://iopscience.iop.org/article/10.1149/2.002405jss/meta. Publisher: IOP Publishing.

[13] Yersak, Alexander S., Lee, Yung C., Spencer, Joseph A. and Groner, Markus D. "Atmospheric pressure spatial atomic layer deposition web coating with in situ monitoring of film thickness." *Journal of Vacuum Science & Technology A* Vol. 32 No. 1 (2013): p. 01A130. DOI 10.1116/1.4850176. Accessed 2023-09-22, URL https://doi.org/10.1116/1.4850176.

[14] Levy, David H., Freeman, Diane, Nelson, Shelby F., Cowdery-Corvan, Peter J. and Irving, Lyn M. "Stable ZnO thin film transistors by fast open air atomic layer deposition." *Applied Physics Letters* Vol. 92 No. 19 (2008): p. 192101. DOI 10.1063/1.2924768. Accessed 2023-09-22, URL https://doi.org/10.1063/1.2924768.

[15] Levy, David H., Nelson, Shelby F. and Freeman, Diane. "Oxide Electronics by Spatial Atomic Layer Deposition." *Journal of Display Technology* Vol. 5 No. 12 (2009): pp. 484–494. DOI 10.1109/JDT.2009.2022770. Conference Name: Journal of Display Technology.

[16] Mousa, Moataz Bellah M., Ovental, Jennifer S., Brozena, Alexandra H., Oldham, Christopher J. and Parsons, Gregory N. "Modeling and experimental demonstration of high-throughput flow-through spatial atomic layer deposition of Al2O3 coatings on textiles at atmospheric pressure." *Journal of Vacuum Science & Technology A* Vol. 36 No. 3

(2018): p. 031517. DOI 10.1116/1.5022077. Accessed 2023-09-22, URL https://doi.org/10.1116/1.5022077.

[17] Choi, Hagyoung, Shin, Seokyoon, Jeon, Hyeongtag, Choi, Yeongtae, Kim, Junghun, Kim, Sanghun, Chung, Seog Chul and Oh, Kiyoung. "Fast spatial atomic layer deposition of Al2O3 at low temperature (<100 °C) as a gas permeation barrier for flexible organic light-emitting diode displays." *Journal of Vacuum Science & Technology A* Vol. 34 No. 1 (2015): p. 01A121. DOI 10.1116/1.4934752. Accessed 2023-09-22, URL https://doi.org/10.1116/1.4934752.

[18] Muñoz-Rojas, David, Sun, Haiyan, Iza, Diana C., Weickert, Jonas, Chen, Li, Wang, Haiyan, Schmidt-Mende, Lukas and MacManus-Driscoll, Judith L. "High-speed atmospheric atomic layer deposition of ultra thin amorphous TiO2 blocking layers at 100 °C for inverted bulk heterojunction solar cells." *Progress in Photovoltaics: Research and Applications* Vol. 21 No. 4 (2013): pp. 393–400. DOI 10.1002/pip.2380. Accessed 2023-09-22, URL https://onlinelibrary.wiley.com/doi/abs/10.1002/pip.2380. _eprint: https://onlinelibrary.wiley.com/doi/pdf/10.1002/pip.2380.

[19] Sekkat, Abderrahime, Nguyen, Viet Huong, Masse de La Huerta, César Arturo, Rapenne, Laetitia, Bellet, Daniel, Kaminski-Cachopo, Anne, Chichignoud, Guy and Muñoz-Rojas, David. "Open-air printing of Cu2O thin films with high hole mobility for semitransparent solar harvesters." *Communications Materials* Vol. 2 No. 1 (2021): pp. 1–10. DOI 10.1038/s43246-021-00181-8. Accessed 2023-09-22, URL https://www.nature.com/articles/s43246-021-00181-8. Number: 1 Publisher: Nature Publishing Group.

[20] Zhao, Ming-Jie, Sun, Zhi-Tao, Hsu, Chia-Hsun, Huang, Pao-Hsun, Zhang, Xiao-Ying, Wu, Wan-Yu, Gao, Peng, Qiu, Yu, Lien, Shui-Yang and Zhu, Wen-Zhang. "Zinc Oxide Films with High Transparency and Crystallinity Prepared by a Low Temperature Spatial Atomic Layer Deposition Process." *Nanomaterials* Vol. 10 No. 3 (2020): p. 459. DOI 10.3390/nano10030459. Accessed 2023-09-22, URL https://www.mdpi.com/2079-4991/10/3/459. Number: 3 Publisher: Multidisciplinary Digital Publishing Institute.

[21] Hsu, Chia-Hsun, Zhu, Run-Feng, Kang, Pin-Chun, Gao, Peng, Wu, Wan-Yu, Wuu, Dong-Sing, Lien, Shui-Yang and Zhu, Wen-Zhang. "Low-temperature spatial atomic layer deposited Ga2O3 films for high-performance flexible deep ultraviolet photodetector." *Materials Letters* Vol. 340 (2023): p. 134204. DOI 10.1016/j.matlet.2023.134204. Accessed 2023-09-22, URL https://www.sciencedirect.com/science/article/pii/S0167577X23003890.

[22] Gurbandurdyyev, Guvanch, Mistry, Kissan, Delumeau, Louis-Vincent, Loke, Jhi Yong, Teoh, Chee Hau, Cheon, James, Ye, Fan, Tam, Kam Chiu and Musselman, Kevin P. "Robust, Conformal ZnO Coatings on Fabrics via Atmospheric-Pressure Spatial Atomic Layer Deposition with In-Situ Thickness Control**." *ChemNanoMat* Vol. 9 No. 2 (2023): p. e202200498. DOI 10.1002/cnma.202200498. Accessed 2023-09-22, URL https://onlinelibrary.wiley.com/doi/abs/10.1002/cnma.202200498. _eprint: https://onlinelibrary.wiley.com/doi/pdf/10.1002/cnma.202200498.

[23] Ryan Fitzpatrick, P., Gibbs, Zachary M. and George, Steven M. "Evaluating operating conditions for continuous atmospheric atomic layer deposition using a multiple slit gas source head." *Journal of Vacuum Science & Technology A* Vol. 30 No. 1 (2011): p. 01A136. DOI 10.1116/1.3664765. Accessed 2023-09-22, URL https://doi.org/10.1116/1.3664765.

[24] Deng, Zhang, He, Wenjie, Duan, Chenlong, Chen, Rong and Shan, Bin. "Mechanistic modeling study on process optimization and precursor utilization with atmospheric spatial atomic layer deposition." *Journal of Vacuum Science & Technology A* Vol. 34 No. 1 (2015): p. 01A108. DOI 10.1116/1.4932564. Accessed 2023-09-22, URL https://doi.org/10.1116/1.4932564.

[25] de la Huerta, Cesar Arturo Masse, Nguyen, Viet H., Sekkat, Abderrahime, Crivello, Chiara, Toldra-Reig, Fidel, Veiga, Pedro Brandao, Quessada, Serge, Jimenez, Carmen and Muñoz-Rojas, David. "Gas-Phase 3D Printing of Functional Materials." *Advanced Materials Technologies* Vol. 5 No. 12 (2020): p. 2000657. DOI 10.1002/admt.202000657. Accessed 2023-09-22, URL https://onlinelibrary.wiley.com/doi/abs/10.1002/admt.202000657. _eprint: https://onlinelibrary.wiley.com/doi/pdf/10.1002/admt.202000657.

[26] Midani, Laabdia, Ben-Yahia, Waël, Salles, Vincent and Marichy, Catherine. "Nanofabrication via Maskless Localized Atomic Layer Deposition of Patterned Nanoscale Metal Oxide Films." *ACS Applied Nano Materials* Vol. 4 No. 11 (2021): pp. 11980–11988. DOI 10.1021/acsanm.1c02550. Accessed 2023-09-22, URL https://doi.org/10.1021/acsanm.1c02550. Publisher: American Chemical Society.

[27] Dickey, Eric and Barrow, William A. "High rate roll to roll atomic layer deposition, and its application to moisture barriers on polymer films." *Journal of Vacuum Science & Technology A* Vol. 30 No. 2 (2012): p. 021502. DOI 10.1116/1.3678486. Accessed 2023-09-22, URL https://doi.org/10.1116/1.3678486.

[28] Li, Zoushuang, Cao, Kun, Li, Xiaobo and Chen, Rong. "Computational fluid dynamics modeling of spatial atomic layer deposition on microgroove substrates." *International Journal of Heat and Mass Transfer* Vol. 181 (2021): p. 121854. DOI 10.1016/j.ijheatmasstransfer.2021.121854. Accessed 2023-09-22, URL https://www.sciencedirect.com/science/article/pii/S0017931021009595.

[29] Tom, Matthew, Yun, Sungil, Wang, Henrik, Ou, Feiyang, Orkoulas, Gerassimos and Christofides, Panagiotis D. "Multiscale Modeling of Spatial Area-Selective Thermal Atomic Layer Deposition." Kokossis, Antonios C., Georgiadis, Michael C. and Pistikopoulos, Efstratios (eds.). *Computer Aided Chemical Engineering*. Vol. 52 of *33 European Symposium on Computer Aided Process Engineering*. Elsevier (2023): pp. 71–76. DOI 10.1016/B978-0-443-15274-0.50012-3. Accessed 2023-11-15, URL https://www.sciencedirect.com/science/article/pii/B9780443152740500123.

[30] Masse de la Huerta, César, Nguyen, Viet Huong, Dedulle, Jean-Marc, Bellet, Daniel, Jiménez, Carmen and Muñoz-Rojas, David. "Influence of the Geometric Parameters on the Deposition Mode in Spatial Atomic Layer Deposition: A Novel Approach to Area-Selective Deposition." *Coatings* Vol. 9 No. 1 (2019): p. 5. DOI 10.3390/coatings9010005. Accessed 2023-09-22, URL https://www.mdpi.com/2079-6412/9/1/5. Number: 1 Publisher: Multidisciplinary Digital Publishing Institute.

[31] Yun, Sungil, Tom, Matthew, Orkoulas, Gerassimos and Christofides, Panagiotis D. "Multiscale computational fluid dynamics modeling of spatial thermal atomic layer etching." *Computers & Chemical Engineering* Vol. 163 (2022): p. 107861. DOI 10.1016/j.compchemeng.2022.107861. Accessed 2023-11-15, URL https://www.sciencedirect.com/science/article/pii/S0098135422001995.

[32] Penley, Daniel, Cho, Tae H., Brooks, Andre J., Ransohoff, Lauren, Park, Hyunwoo, Zhao, Enpei, Trejo, Orlando, Barton, Kira and Dasgupta, Neil P. "Mechatronic Spatial Atomic Layer Deposition for Closed-Loop and Customizable Process Control." *Advanced Materials Technologies* (2024): p. 2301728.

[33] Penley, Daniel and Dasgupta, Neil P. "Spatial Atomic Layer Deposition: Experimental Validation of Simulated Deposition Maps." Vol. In preparation .

APPENDIX A. APPENDIX

TABLE 2: Process Parameters for Model and Experimental System

Parameter	Values	Units	Ref.
l	7.62	mm	Experimental
d	1.016	mm	Experimental
h	2.5	mm	Experimental
w	114.3	mm	Experimental
Δz	1	mm	Experimental
$Q_{\mathrm{N_2\text{-}out}}$	284.1	sccm	Experimental
$Q_{\mathrm{N_2\text{-}in}}$	238.1	sccm	Experimental
Q_{exh}	162.5	sccm	[32]
Q_{TTIP}	48.33	sccm	Experimental
$Q_{\mathrm{H_2O}}$	57.14	sccm	Experimental
$\dot{n}_{\mathrm{TTIP}}$	1.75E-8	mol s^{-1}	[33]
$\dot{n}_{\mathrm{H_2O}}$	9.30E-6	mol s^{-1}	[33]
D_{TTIP}	0.083	$\mathrm{cm}^2\ \mathrm{s}^{-1}$	[33]
$D_{\mathrm{H_2O}}$	0.395	$\mathrm{cm}^2\ \mathrm{s}^{-1}$	[33]
T	378.15	K	Experimental
v	10	mm s^{-1}	Experimental
L_{travel}	18	mm	Experimental